Calculation of Land Surface Temperature Using a Generalized Split-Window Algorithm and the Reconstruction of its Lost Data by Cloud Cover Through a Singular Spectral Analysis (SAA) algorithm

Hadi Zare Khormizi[1*] ⓘ ✉, Hamid Reza Ghafarian Malamiri[2] ⓘ, Sahar Alian[3] ⓘ

[1] Faculty of Natural Resources, University of Tehran, Karaj, Iran. Email: hadi.zarekh@ut.ac.ir
[2] Department of Geography, Yazd University, Yazd, Iran.
[3] Department of Civil Engineering, Rahman Institute of Higher Education, Ramsar, Iran.

Article Info.	ABSTRACT
Article type: Research Article **Article history:** Received: 16 Nov. 2022 Received in revised from: 13 May 2023 Accepted: 09 June 2023 Published online: 27 June 2023 **Keywords:** Time series, split-window algorithm, singular spectrum analysis, spatio-temporal interpolation, Landsat 8.	Land Surface Temperature (LST) is one of the most important parameters in land-atmosphere energy exchange that is applicable to many sciences such as climatology, hydrology, agriculture, ecology, etc. One of the most significant limitations of using remote sensing for estimation of LST is the presence of clouds, which remarkably affects the energy reflected from the surface and disrupts the reading ability of the optical and thermal sensors. In the present study, 23 Landsat 8 images in 2015 were used as an annual time series to estimate LST in a part of the pistachio farms of Yazd, Iran. LST in the 23 images was estimated by generalized split-window algorithm. The results showed in the estimated (23 images) LST time series, the minimum, maximum, and mean missing data due to cloud cover were 17%, 28%, and 19%, respectively. SSA algorithm was used to solve the problem of missing data. Root Mean Square Error (RMSE) and Mean Absolute Error (MAE) between the original and reconstructed data at the data points in the studied LST time series were 3.4 and 2.5 K, respectively. Moreover, the gap-filling error was estimated by extracting five random images with four iterations of time series and comparing the reconstructed images with the extracted spatio-temporal images. RMSE and MAE were estimated to be 4.4 and 3.6 K in reconstruction of temporal artificial gaps and 3.7 and 2.8 K in the spatial artificial gaps, respectively. Based on the findings, SSA algorithm can be effectively used to fill the problem of missing data due to cloud cover in Landsat 8 LST time series.

1. Introduction

Land Surface Temperature (LST) is one of the most significant physical parameters used for evaluation of land-atmosphere energy exchange (Sobrino *et al*., 2003; Ghafarian *et al*., 2012; Xu and Shen, 2013). This parameter is applicable to many different domains, such as climatology, hydrology, agriculture, ecology, and environmental sciences modelling, in which continuous and consistent LST time series as the input data are very important (Tatem *et al*., 2004; Sun *et al*., 2004; Estes *et al*., 2009; Teixeira, 2010; Costa *et al*., 2019). One of the methods used for estimation of LST is the use of satellite data and thermal remote sensing techniques. The LST estimation techniques make use of the data of thermal infrared bands. Scholars worldwide have proposed various LST retrieval algorithms from thermal infrared bands, which include the Mono-Window Algorithm (MWA), Radiative Transfer Equation (RTE), Split-Window Algorithm (SWA), Single-Channel Algorithm (SCA), Multi-Angle Algorithm, Multi-Channel Algorithm, and Hyperspectral Algorithm (Sekertekin and Bonafoni, 2020; Jiang and Lin, 2021). The most common algorithm is the split-window algorithm, which estimates LST by a linear or nonlinear combination of the brightness temperature of two thermal bands (i.e. bands 11 and 12 of Landsat 8) (Becker *et al*., 1995).

The split-window algorithm makes it possible to estimate the LST by using land cover data, brightness temperature captured by thermal sensor, Land Surface Emissivity (LSE), and Fractional Vegetation Cover (FVC) (Latif, 2014). Numerous studies have used split-window algorithm for estimation of LST (Wang *et al*., 2019; Sajib and Wang, 2020; Sekertekin and Bonafoni, 2020; Jiang and Lin, 2021). Jiang and Lin (2021) compared the accuracy of LST estimation methods obtained from Landsat 8 images in China including: mono-window algorithm, radiative transfer equation, split-window algorithm, single-channel algorithm. The results showed that the split-window algorithm had higher accuracy in the summer season. Wang *et al*. (2019) compared three LST estimation algorithms using Landsat 8 images. In this research, the mono-window algorithm, the split window algorithm, and the single-channel methods were investigated to estimate the LST. The results showed that all three algorithms have high accuracy for estimating the temperature of the earth's surface. A study used a split-window and a single-channel algorithm to estimate LST from the thermal images of Landsat 8. The results showed split-window algorithm provided better results than single-channel algorithm during increased atmospheric water vapor (Jiménez-Muñoz *et al*., 2014). Another study used the split-window algorithm to estimate LST by Landsat 8 data. The findings indicated the LST inverted from the radiative transfer equation-based method using band 10 had the highest accuracy, split-window algorithm had average accuracy, and single-channel algorithm had the lowest accuracy (Yu *et al*., 2014). Feizizadeh *et al*. (2016) used multispectral and thermal images of Landsat 8 for estimation of LST using split-window algorithm in Mahabad catchment. They reported that split-window algorithm could yield reliable results in estimation of LST. Moreover, Rahimian *et al*. (2017) evaluated different methods used for estimation of the vegetation temperature of pistachio trees using Landsat 8 images. They found split-window algorithm was more accurate than single-window, modified single-window, and single-channel algorithms.

As for the use of remote sensing techniques for estimation of LST, factors such as atmospheric dust, aerosols, gases, sensor malfunction and clouds, in particular, can significantly influence the energy radiated from the surface and disrupt the reading potential of the thermal sensors (Julien and Sobrino, 2010). These cause gaps (no data) e.g. due to cloud removal algorithm in preprocessing, and outliers (data higher or lower than surrounding) due to e.g. sensor malfunction in LST data. In both cases, we have data contaminated by zero or NaN and incorrect values. Clouds have higher reflection in the visible bands of the electromagnetic

spectrum and usually lower temperature in the thermal bands than the land surface below them (Ackerman *et al*., 2006). In remote sensing, clouds absorb a part of thermal energy radiated from the land. They also emit very low thermal infrared energy (Ghafarian Malamiri, 2015). This makes the remote sensing techniques unable to measure the actual LST anytime and anywhere because of the effect of cloud cover. Therefore, gaps and outliers will exist in LST time series. Hence, obtaining continuous and cloudless datasets remains challenging for researchers.

More than 20 techniques have been used to remove lost (gap) and outlier data caused by cloud coverage in time series data (LST or NDVI), (Jeng *et al*., 2014). These techniques can be divided into three categories: temporal, spatial, and temporal-spatial (Chen *et al*., 2022). For example, Fast Fourier Transform (FFT) algorithm and Harmonic ANalysis of Time Series (HANTS) algorithm have been used based on the temporal approach for reconstruction of time series with gaps and outliers for NDVI and LST (Menenti *et al*., 1993; Verhoef, 1996; Verhoef *et al*., 1996; Zhou *et al*., 2015; Zare khormizi and Ghafarian Malamiri, 2020, Ghafarian Malamiri and Zare Khormizi, 2020). Spatial methods such as linear regression and quadratic polynomial regression (Mukherjee *et al*., 2014) and Multi- Single Spectrum Analysis (M-SSA) algorithm can be mentioned as temporal-spatial methods (Ghafarian Malamiri *et al*., 2018).

Ghafarian and Zare Khormizi (2017) studied the capability of HANTS algorithm in the reconstruction of daily MODIS LST time series. Their findings showed RMSE values of 3.87 and 2.68 K between the original data and reconstructed data in LST time series during the day and night, respectively. Jeng *et al*. (2014) used eight different techniques including the modified best index slope extraction (M-BISE) technique, the Savitzky-Golay (SG) technique, the Mean Value Iteration filter (MVI) technique, the Asymmetric Gaussian (AG) technique, the Double Logistic (DL) technique, the Changing-Weight filter (CW) technique, the Interpolation for Data Reconstruction (IDR) technique, and the Whittaker Smoother (WS) technique, performed better than other tested techniques. Julien and Sobrino (2010) investigated three reconstruction methods (IDR, HANTS, 2LOG) in research to reconstruct the effects of cloud cover in NDVI time series. In this study, it was shown that the IDR method produces better result than others in most cases. Chen *et al*. (2022) compared the temporal, spatial and spatio-temporal reconstruction methods in MODIS land surface temperature in cloudy conditions. Based on the results, the linear temporal interpolation method using Aqua data had the better performance in MODIS LST reconstruction in the Heihe river basin, China, with the RMSE of 7.13 K. Zhou *et al*. (2016) evaluated the reconstruction performance of five different methods of harmonic analysis, double logistic, asymmetric gaussian, whittaker smoother and savitzky–golay filter in reconstructing NDVI time series. Based on the results of this study, taking into account the overall reconstruction error, the asymmetric gaussian model performs better than other models in regions with high-latitude, while the savitzky-golay model has the best reconstruction performance in tropical and subtropical regions. Cai *et al*. (2017) investigated the performance of smoothing methods for reconstructing NDVI time series. In this review, five methods, savitzky-golay fitting, locally weighted regression scatterplot smoothing (LO), spline smoothing (SP), asymmetric gaussian function fitting, and double logistic function fitting were compared. The results show that all smoothing methods can reduce noise and improve signal quality, but no method always performs better than others.

Based on the literature review, two important points can be mentioned. 1. most of the methods used in the field of data reconstruction lost by cloud cover are based on temporal behavior of a time series. 2. According to the type of time series, the amount of missing data and the study area, the best reconstruction method is different. However, one of the unknown methods of reconstructing lost data in time series is the Single Spectrum Analysis (SSA)

algorithm.

The Single Spectrum Analysis (SSA) algorithm is an advanced method for reconstructing time series with lost data; which uses temporal correlation (single channel: SSA) and temporal-spatial correlation (multi-channel: M-SSA). SSA was first developed by Broomhead and King (1986). It was then suggested by Vautard and Ghil (1992) and Kondrashov and Ghil (2006) for filling the gaps in time series. LST time series have periodic data (signals or cycles data) and noises. Cycles result from the Earth's rotation around the sun, seasonal variations occur due to deviation of the Earth's axis, and noises happen due to interactions between radiant energy, atmosphere and turbulent energy in the environment. Assuming this, SSA uses Empirical Orthogonal Functions (EOFs) and analysis of main temporal components to extract data from the time series (Vautard and Ghil, 1992). SSA is an advanced method for analysis of time series that makes use of the principles of multivariate statistics and geometry, linear algebra, and signal processing (Golyandina and Zhigljavsky, 2013). This algorithm analyzes a time series into simpler and interpretable components such as trends, cyclic and semi-cyclic variations, and noises (Golyandina *et al.*, 2001). Therefore, in time series data, some important and significant components have the highest variance and noise has the lowest variance in the observations.

SSA has been used as a standard tool for the analysis of climatic, hydrologic, meteorological, and geophysical time series (Vautard and Ghil., 1989; Ghil and Vautard., 1991; Yiou *et al.*, 1996; Yiou *e al.*, 2000; Kondrashov *et al.*, 2010). Yet, this algorithm has not been used much for the reconstruction of remote sensing time series. Ghafarian *et al.* (2012) reconstructed the three-years of hourly LST time series in Tibetan plateau using M-SSA and reported the average of the MAE of 2.25 K between original and reconstructed time series. The overall temporal average of gaps was 63% due to cloud cover. Further, Wang and Liang. (2008) used M-SSA for reconstruction of missing data in MODIS Leaf Area Index (LAI). Their results showed M-SSA was effective in reconstruction of this index using spatio-temporal correlation. In addition, Ghafarian Malamiri *et al.* (2018) assessed the ability of M-SSA in reconstruction of missing data due to cloud cover in daily MODIS time series using 730 data per year (day and night data). They reported the RMSE of 2.95 K between the original data and reconstructed data. Ghafarian Malamiri *et al.* (2020) compared HANTS (temporal) and M-SSA (temporal-spatial) algorithms in reconstructing missing data with large and continuous gaps in NDVI time series. The results showed that the RMSE between the original and reconstructed data in HANTS and M-SSA algorithms is 0.027 and 0.023 of NDVI, respectively. In addition, the RMSE error among 15 NDVI images extracted from time series artificially and reconstructed by HANTS and M-SSA algorithms were 0.03 and 0.025 NDVI value, respectively. Based on the results of this research, the M-SSA algorithm is more preferable than the HANTS algorithm for reconstructing lost data with long gaps (due to several cloudy days).

The main objective of present study is to evaluate the performance of (M)-SSA in the reconstruction of missing data due to cloud cover in Landsat 8 LST time series. In most applied studies on remote sensing by LST images, cloud cover has always been considered a limitation in selecting the images. Therefore, this research can be used in most applied studies on LST images owing to the pure data generated by (M)-SSA algorithm.

2. Materials and methods
2.1. Study area
This study was conducted in 20 km south of Dehshir rural district, Yazd province. This region is located between $31° 12' 47''$ and $31° 19' 09''$ latitudes and $53° 39' 47''$ and $53° 47' 15''$ longitudes.

The study area is 13971 ha. In terms of topography, the studied area is almost plain and flat,

and the average height above sea level is 1500 m. The amount of rainfall in the study area is less than 100 mm per year. The average cloudy days in this region is about 50 days (≈ 1180 hours). This region is covered mostly with pistachio orchards. Fig. 1 illustrates the study location in Iran and Yazd province along with a false-color composite image.
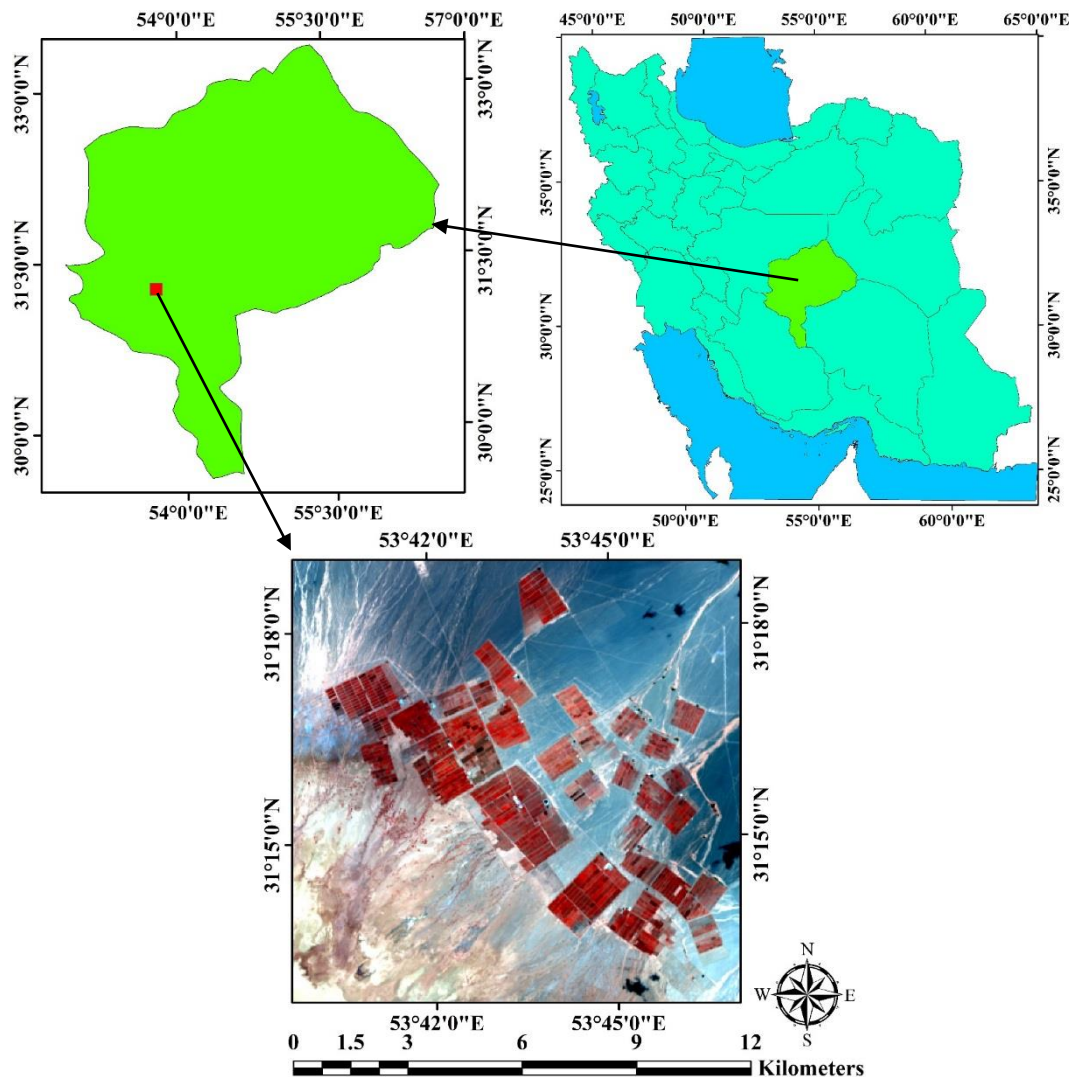

Fig. 1. Study location in Iran and Yazd province

2.2. *Satellite data*

In this study, Landsat 8 data were used. Landsat 8 carries two sensors, Operational Land Imager (OLI) and Thermal Infrared Sensor (TIRS). The OLI collects data with spatial resolution of 30 m and 8 bands in visible spectrum, near infrared, short-wave infrared, and a panchromatic band with spatial resolution of 15 m. TIRS records the thermal infrared radiations with spatial resolution of 100 m using two bands in atmospheric windows 10.6-11.2 µm for band 10 and 11.5-12.5 µm for band 11 (Irons *et al*., 2012; Wang *et al*., 2015). In the present study, 23 Landsat 8 images in 2015 were used in a time series to estimate the LST. The images taken on 2015/01/27, 2015/03/16, 2015/04/01, and 2015/05/03 are completely cloudy and those taken on 2015/12/12, 2015/07/06, and 2015/07/22 images are partly cloudy. The first two digits from the right show the day, the second two digits show the month, and the last four digits represent

the year. Table 1 presents the dates of the images used.

Table 1. The dates of the images (0000.00.00 = year month day)

Date of image	Date of image	Date of image
2015/01/11	2015/05/19	2015/09/24
2015/01/27	2015/06/04	2015/10/10
2015/02/12	2015/06/20	2015/10/26
2015/02/28	2015/07/06	2015/11/11
2015/06/03	2015/04/22	2015/11/27
2015/04/01	2015/08/07	2015/12/13
2015/04/17	2015/08/23	2015/12/29
2015/05/03	2015/09/08	

2.3. Estimation of Land Surface Temperature (LST)
The following steps were gone through to estimate the LST by split-window algorithm.

2.3.1. Estimation of Normalized Difference Vegetation Index (NDVI)
Since vegetation plays a pivotal role in the land-atmosphere energy exchange, it can be considered a crucial factor in the estimation of LST. NDVI is a widely used index among remote sensing vegetation indices. It was estimated by Eq. 1 for all 23 Landsat 8 images taken in 2015 (Rouse *et al.*, 1973).

$$NDVI = \frac{P\ NIR - P\ RED}{P\ NIR + P\ RED} \tag{1}$$

In this equation, *P NIR* and *P RED* represent near-infrared reflectance band (band 5 of Landsat 8) and red reflectance band (band 4 of Landsat 8), respectively. The obtained range from this index is variable from -1 to +1. Considering the 16-day return period of Landsat 8, the annual NDVI time series includes 23 images. Since NDVI is a factor required for estimation of LST, the gap due to cloud cover (the so-called cloudy images) in annual NDVI time series was first reconstructed by HANTS algorithm. Table 2 presents the parameters used in HANTS algorithm for reconstruction of annual NDVI time series. Given the lengthy discussion of HANTS algorithm, further information can be obtained via studies conducted by Zare Khormizi *et al.* (2017) and Ghafarian and Zare Khormizi (2017).

Table 2. Parameters used for reconstruction of NDVI images by HANTS algorithm

Parameter	Rate
Valid data range	0-1
Basic period	23 NDVI images
Number Of Frequencies(NOF)	3.00
Fit Error Tolerance(FET)	0.02
Direction of outliers	LOW
Degree of Over Determinedness (DOD)	5.00

2.3.2. Estimation of Fractional Vegetation Cover (FVC)

FVC is a parameter that is used in many environmental applications and climatic variations. A common approach for estimation is a nonlinear combination of two spectral elements in a remote sensing image, including bare soil and green vegetation. The spectral features of these two elements are usually estimated in different ways, including filed measurement, estimation of additional data sources, or directly from the extracted images (Johnson *et al.*, 2015). FVC is calculated by the following relation (Sobrino *et al.*, 2008; Latif, 2014):

$$FVC = \frac{NDVI - NDVI_s}{NDVI_v - NDVI_s}$$
(2)

where *NDVI* is the value of pixels in the index, *NDVIs* represents areas with no vegetation, and *NDVIv* shows areas with vegetation.

2.3.3. Estimation of Land Surface Emissivity (LSE)

Another parameter required for estimation of LST is estimation of LSE, which was estimated separately in both thermal bands of Landsat 8. LSE is computed by Eq. 3 (Sobrino *et al.*, 2008; Latif, 2014).

$$LSE = E^S(1 - FVC) + E^V \times FVC$$
(3)

In this equation, *LSE* is land surface emissivity, *FVC* is fractional vegetation cover, and E^S and E^V show emissivity of soil and vegetation, respectively (Table 3).

Table 3. Emissivity of soil and vegetation (Skoković *et al.*, 2014; Latif, 2014)

Emissivity	Band 10	Band 11
(emissivity of vegetation) E^V	0.987	0.989
(emissivity of soil) E^S	0.971	0.977

After estimating the LSE, the mean and difference of LSE for bands 10 and 11 were calculated by the Eq. 4 and 5, respectively (Latif, 2014).

$$Mean, LSE = m = \frac{LSE_{10} + LSE_{11}}{2}$$
(4)

$$\Delta LSE = \Delta m = LSE_{10} - LSE_{11}$$
(5)

2.3.4. Estimation of brightness temperature

The thermal band data can be converted into brightness temperature using thermal constant in the metadata file. To this end, the radiance of thermal bands was first estimated by equation 6 (Latif, 2014).

$$L^\lambda = M_L \times Q_{cal} + A_L$$
(6)

In this equation, L^λ is top-of-atmosphere (TOA) radiance (Watts/m^2×srad×μm), M_L is

radiance-multi-band-10/11, which is obtained from metadata file, Q_{cal} is the targeted band, and A_L is radiance-add-band-10/11, which is extracted from the metadata file.

After estimating the TOA radiance, the brightness temperatures of bands 10 and 11 were estimated by equation 7 (Latif, 2014).

$$TB = \frac{K_2}{\ln(\frac{k_1}{L^\lambda}+1)}$$

(7)

In this relation, TB is TOA brightness temperature, K_1 and K_2 are thermal constants of both bands based on the metadata file, and L^λ is TOA radiance.

2.3.5. Estimation of Column Water Vapor (CWV)
CWV plays a key role in improving the accuracy and estimation of LST, which is calculated by relation 8 (Li $et\ al.$, 2003; Du $et\ al.$, 2015).

$$CWV = C_0 + C_1(\tau_j / \tau_i) + C_2(\tau_j / \tau_i)^2$$

(8)

$$(\tau_j / \tau_i) \approx R_{ji} = \frac{\sum_{k=1}^{N}(T_{i,k} - \overline{T_i})(T_{j,k} - \overline{T_j})}{\sum_{k=1}^{N}(T_{i,k} - \overline{T_i})^2}$$

(9)

In Equations (8, 9), C_0, C_1 and C_2 are the coefficients obtained from the simulated data; τ is the band effective atmospheric transmittance; N is the number of adjacent pixels in a spatial window size n ($i.e.$, $N = n \times n$); $T_{i,k}$ and $T_{j,k}$ are the respective brightness temperatures (K) of bands i and j at the TOA level for the kth pixel; and $\overline{T_i}$ and $\overline{T_j}$ are the mean or median brightness temperatures of the N pixels for the two bands.

2.3.6. Split-window algorithm
This algorithm is one of the methods used for estimation of LST that has higher accuracy than other methods in estimating LST. LST is estimated by this algorithm via Eq. 10 (Latif, 2014; Sobrino $et\ al.$, 1996).

$$LST = TB_{10} + C_1(TB_{10} - TB_{11}) + C_2(TB_{10} - TB_{11})^2 + C_0 + (C_3 + C_4 W)(1-m) + (C_5 + C_6 W)\Delta m$$

(10)

In this relation, LST is land surface temperature, $TB10$ and $TB11$ are brightness temperatures of bands 10 and 11, W is column water vapor, m is mean land surface emissivity, $m\Delta$ is land surface emissivity difference, and C_0-C_6 are coefficients of the algorithm (Table 4).

Table 4. Split-window algorithm coefficients (Skoković $et\ al.$, 2014; Latif, 2014)

Coefficients	C_0	C_1	C_2	C_3	C_4	C_5	C_6
Values	-0.268	1.387	0.183	54.300	-2.238	-129.200	16.400

Based on the stages described, Fig. 2 illustrates a flowchart of the stages of LST estimation by split-window algorithm.
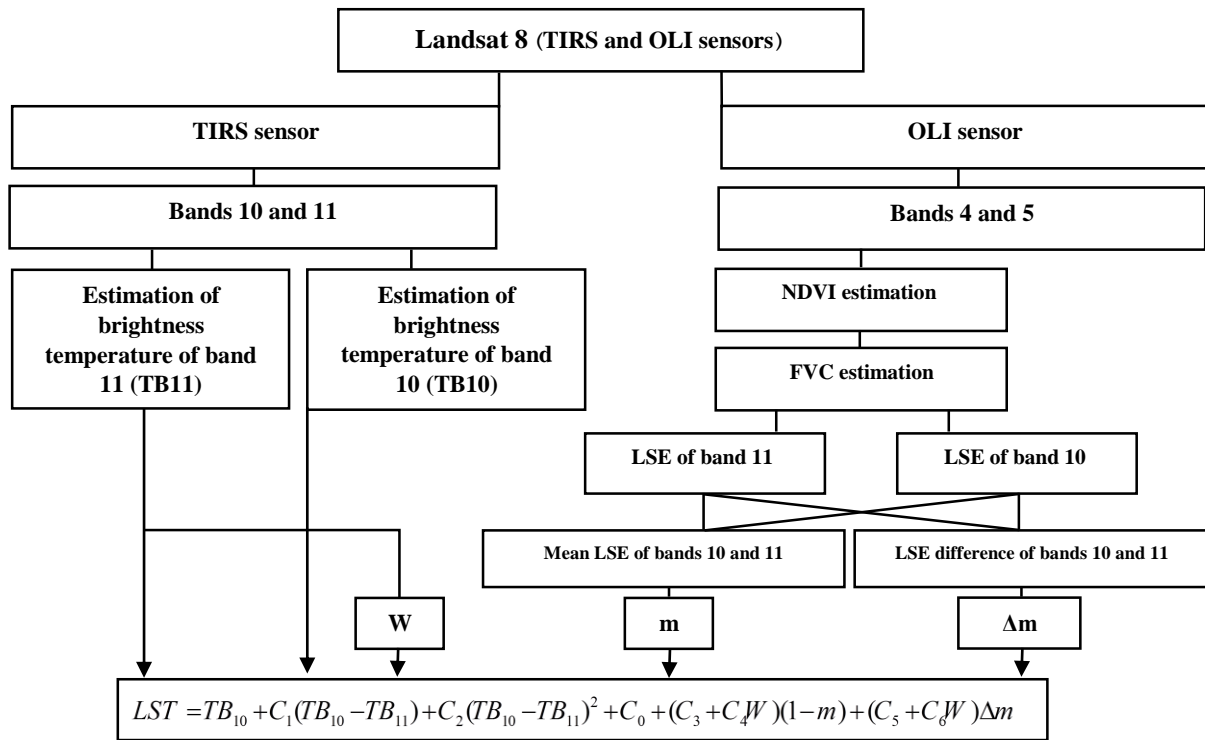
Fig. 2. A simple workflow of estimation of LST by split-window algorithm

2.4. Singular Spectrum Analysis algorithm

The procedure of gap-filling is based on using SSA and smoothing algorithm (Ghafarian *et al.*, 2012, Musial *et al.*, 2011). Thae main basis of SSA is based on construction of Singular Value Decomposition (SVD), which is a well-known factorization matrix process. The remote sensing application of SVD has been proved in many studies such as feature extraction (Izquierdo Verdiguier, 2014) or spatio-temporal analysis (Li *et al.*, 2013). The spatio-temporal analysis of time series data in climatology science using SVD is known as Empirical Orthogonal Functions (EOFs). The singular values and vectors as: $X = D \sum E^T$ of the matrix ($X \in R^{m \times k}$) is made up by SVD factorization, where $D \in R^{m \times m}$ is made up by right singular vectors, $E \in R^{K \times K}$ is made up by the left singular vectors and $\sum$ is a diagonal matrix that contains the singular values of *X*. The original data being analysis is a time series array of $x = [x_1, x_2, …, x_n]$, where $k = n - m + 1$, and *n* is the number of observations in time. Therefore, a window size of *m is* used to create the time-delayed embedding of *x* and the trajectory matrix, $X \in R^{n \times m}$:

$$X = \begin{pmatrix} x_1 & x_2 & x_3 & … & x_k \\ x_2 & x_3 & x_4 & … & x_{k+1} \\ x_3 & x_4 & x_5 & … & x_{k+2} \\ … & … & … & … & … \\ x_m & x_{m+1} & x_{m+2} & … & x_n \end{pmatrix}$$

(11)

The trajectory matrix contains the complete record of patterns presented within a window of size *m*. Selection of a large (small) window size will result in the capturing of more (less)

information about the basic pattern of the time series but in later case, we will get more statistical confidence as the structure of time series is captured repeatedly (Elsner and Tsonis, 1996; Ghil *et al*., 2002). The SVD calculates the singular values and vectors of the trajectory matrix by decomposition of X. when the singular values are plotted in descending order, an initial signal (represented by a steep slope) and the noise level (represented by a more or less flat floor), can be observed (Vautard *et al*., 1992). Reconstruction of the time series will be done by using the d singular vectors (with $1 \leq d \leq m$) related to d singular values included in the initial signal.

The principal components are obtain as: $PC = X \cdot D$ where the matrix PC takes the form of a Hankel matrix[1] and fit the trajectory matrices consequently. The final steps to the reconstruction of the temporal series are 1) to invert the projection per each component $X'_j = PC(\cdot, j) \cdot D(\cdot, j)$, where $j = 1, \ldots, m$ and 2) to calculate the average along the anti-diagonals of X'_j: $x'(i,j) = 1/(\# \text{ elements diagk}(X'_j)) \cdot \text{sum}(\text{diagk}(X'_j))$, where diagk is the kth diagonal of the matrix, being $k = (n-m+1)+i$.

The gap filling procedure of the SSA can be described in several steps as follows: the neutral value of the mean is calculated and the missing data is set to zero in order to center the original time series for a given window width (m). The SSA algorithm will be applied iterativly on the zeroed and centered data set to obtain the first leading EOF. The current reconstructed components of EOF are used to apprise the missing values. The SSA algorithm is applied once more on the updated set. The missing values will be updated iteratively until the convergence has been achieved. The former EOFs are kept fixed while the process is repeated for a desired number of EOFs. To obtain the optimum number of dominant SSA modes (EOFs) and window width for gap-filling the cross-validation is applied. In cross-validation, a randomly selected portion of the available data is set as missing data. The optimum window size and EOFs is found when the RMSE error between original and reconstructed data doesn't change significantly.

The M-SSA (multi-channel-SSA) is a generalized form of SSA technique used for gap-filling of multivariate time series (Schoellhamer, 2001). The SSA is proposed to be used for single channel variables (applying to segment of a single pixel time series) and Multi-channel (M-SSA) is considering segments of a time series at multi pixels simultaneously. The SSA then can be used to determine periodic components in a pixel as a representative of whole time series and the M-SSA will be applied to reconstruct the time series using the parameters determined by SSA.

2.5. Methods

SSA-MTM software was used to reconstruct an annual LST time series by 23 images during 2015. To reconstruct the time series in SSA software, it is necessary to determine the number of significant components and window size. To determine these parameters, a single time series (a pixel values in time) with no missing data was first selected as a representative of all pixels. Then, the effects of window size and number of components on the reconstruction of this time series by SSA were determined. Next, the significant components of LST time series were determined by different tests in SSA such as Monte Carlo test, which would be discussed in details in the results section. After estimating the window size and significant components, the

---

[1] A Hankel matrix is a square matrix in which each ascending skew-diagonal from left to right is constant, e.g.:
$$\begin{bmatrix} a & b & c & d & e \\ b & c & d & e & f \\ c & d & e & f & g \\ d & e & f & g & h \\ e & f & g & h & i \end{bmatrix}.$$

time series of the whole image were reconstructed by M-SSA. It should be noted that given the lengthy discussion of SSA tests such as Monte Carlo test and Empirical Orthogonal Function (EOF) analysis tests as well as theoretical discussion of trends and cycles, further information can be obtained through the study of Ghafarian Malamiri (2015).

2.6. Evaluation of results

RMSE and MAE were used to assess the performance of M-SSA in reconstruction of the images of this time series. RMSE and MAE were calculated by Eqs. 12 and 13, where x_i and y_i represent original and reconstructed data, respectively.

$$RMSE = \sqrt{\frac{\sum_{i=1}^{n}(x_i - y_i)^2}{n}}$$

(12)

$$MAE = \frac{1}{n}\sum_{i=1}^{n}|x_i - y_i|$$

(13)

There are two types of error in the reconstruction of time series. The first type is "reconstruction error" at valid data points and the second type is the "gap-filling error" where there are no data. To estimate the reconstruction error at data points, first the cloudy data were eliminated from calculation of goodness of fit parameters (RMSE and MAE.) Then, RMSE and MAE were estimated between the original data at this point and data reconstructed by SSA algorithm along each pixel of this time series. To determine the gap-filling error, the original data are required, since valid data do not exist at points with cloud cover. To do so, five random original images without cloud cover in four iterations of original time series were extracted. Then, five images with no data were replaced instead of these images to be reconstructed by SSA. In this state, the missing data along with pixels in time due to cloud cover plus no data due to extracted images from the original data reached approximately 50 % of all data (see results section). Then, the five original images extracted from the LST time series were replaced by gap-free data, and this new time series was reconstructed by SSA algorithm. Finally, RMSE and MAE between the five original images extracted and five spatio-temporally reconstructed images were estimated. Time error is the same reconstruction error along a pixel of the temporal images extracted, which is the output of an image or map. Spatial error is the same error of each pixel of an image with the pixel of the reconstructed corresponding image, which is eventually one value for each image. This process was performed for the second to fourth iterations, and finally the mean spatio-temporal in gap filling was obtained by SSA algorithm.

3. Results

Based on the stages explained in the materials and methods section, LST was estimated on 23 Landsat 8 images by split-window algorithm during 2015. Fig. 3 (left) depicts an LST image without cloud cover taken on 2015/05/19. The minimum LST on this date was 313 K and maximum LST was 331 K. Fig. 3 (right) illustrates an image with cloud cover taken on 2015/02/12. This image has approximately two types of error. The first error is related to data lost by cloud cover (black areas). The second type of error is related to invalid ground temperature data. These data are not spatially identifiable. When the time series has been drawn along each pixel, these data can be detected and reconstructed as outliers compared to the former and later data.
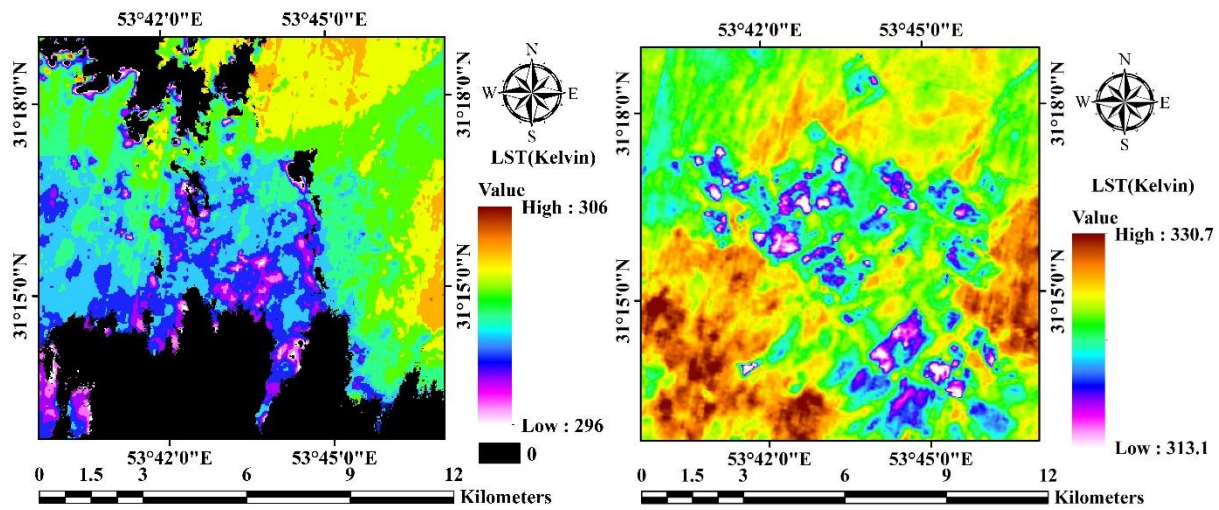
Fig. 3. Two LST images estimated by split-window algorithm on 2015/05/19 (left) and 2015/02/12 (right)

The annual time series of LST images in 2015 was created using the LST images estimated by the split-window algorithm. Then, the time series map of the missing data was drawn by counting the number of missing data along each pixel (Fig. 4, left). As shown, the minimum missing data is 17% and the maximum missing data is 28%, with an average of 19% missing data of this annual time series due to cloud cover. To determine the gap-filling error, five random images with four iterations were extracted from the time series and substituted by images with data. Therefore, the missing data with the same spatial dispersion increased up to 50% (Fig. 4, right).
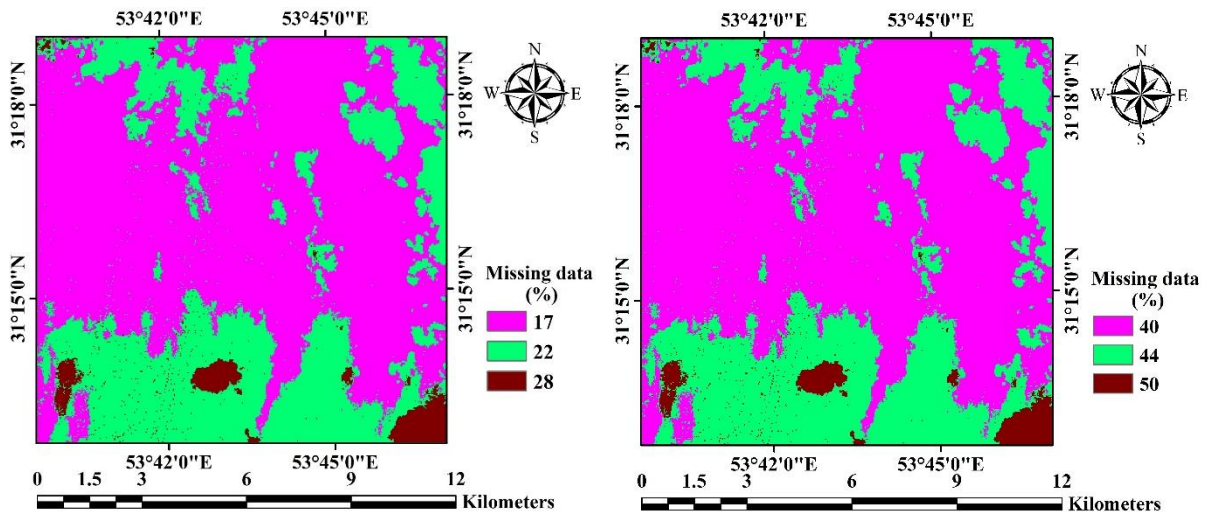

Fig. 4. Missing data due to cloud cover (left) and missing data in time series with four iterations to estimate gap-filling error (right)

3.1. Parameters of SSA algorithm

As stated in the materials and methods section, determining the window size and number of components are important parameters in the reconstruction of time series by SSA algorithm. Thus, first it is necessary to optimally choose the window size and number of components. The

Singular values spectrum with window size of 12 images along a pixel as a representative of the whole time series is depicted in Fig. 5 (left). When the Eigen value curve of a time series is arranged from ascending to descending order, a left-to-right graph with high slope to low-slope areas is obtained. The left side of the graph shows the high slope of the main components of a signal and areas with low slope (graph tail) show noise in the signal. Since the window size 12 images was selected, SSA software divided this time series into 12 parts. Hence, there were 12 states in the horizontal axis. The vertical axis shows the variance effect of the components. As shown in Fig. 5 (left), components 1 and 2 have significantly the highest variance under their control. Since components 1 and 2 are paired, their EOFs are transferred in a quarter phase (phase difference). These components effectively show the cyclic components (Vautard and Ghil, 1989). Figure 5 (right) illustrates the normalized singular values curve in window size of 12 images. As indicated, components 1 and 2 in this time series control 95% of changes (component 1 50% and component 2 45%). On the other hand, failure to select any of these components in the reconstruction of this time series will cause an unacceptable signal.
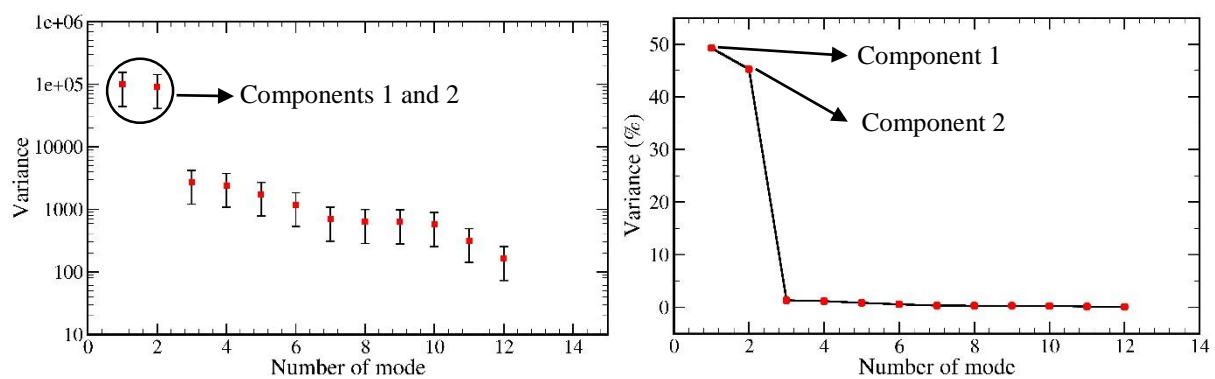

Fig. 5. The Singular values spectrum of data with window size of 12 images (left) and normalized singular values curve (variance changes with respect to each component) in window size of 12 (right)

Figure 6 shows the results of Monte Carlo SSA test with original data. This figure shows the variance values against the given frequency. Components 1 and 2 are the original and significant components of this time series. These two components overlap each other in the figure. The components are named based on larger variance. The frequency of components 1 and 2 is 0.043 cycles per images. Reverse frequency shows the cycle. Therefore, the 23-image cycle is one of the significant cycles of this time series. Since there are 23 LST images in an annual time series, components 1 and 2 indicate the annual cycles of temperature variations.
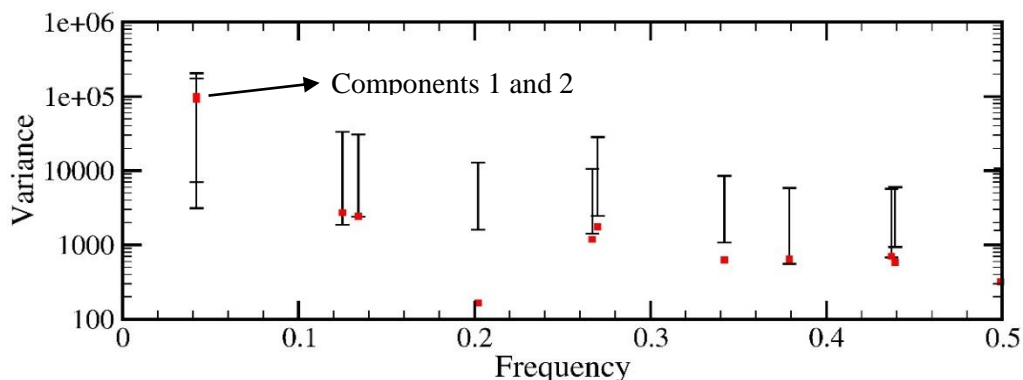

Fig. 6. Monte Carlo SSA based on original data

In general, the results of Monte Carlo and other tests (for the sake of shortness not showing here) showed the use of window size of 12 images yielded reliable results in reconstruction of this time series. In window size of 12 images, two significant components can be differentiated in this time series. Hence, a total of two components and window size of 12 images were considered in M-SSA to reconstruct the entire time series.

3.2. Assessment of the accuracy of images reconstructed by SSA

Figure 7 illustrates the results of a curve fitted by SSA algorithm based on the original LST data along two pixels. As shown, the SSA algorithm has efficiently reconstructed the gaps and outliers in this time series. Further, an ascending temperature trend from the beginning of the time series to its middle and then a descending trend can be observed. This trend is the same annual temperature changes regarded as components 1 and 2 in the significant cyclic components section.
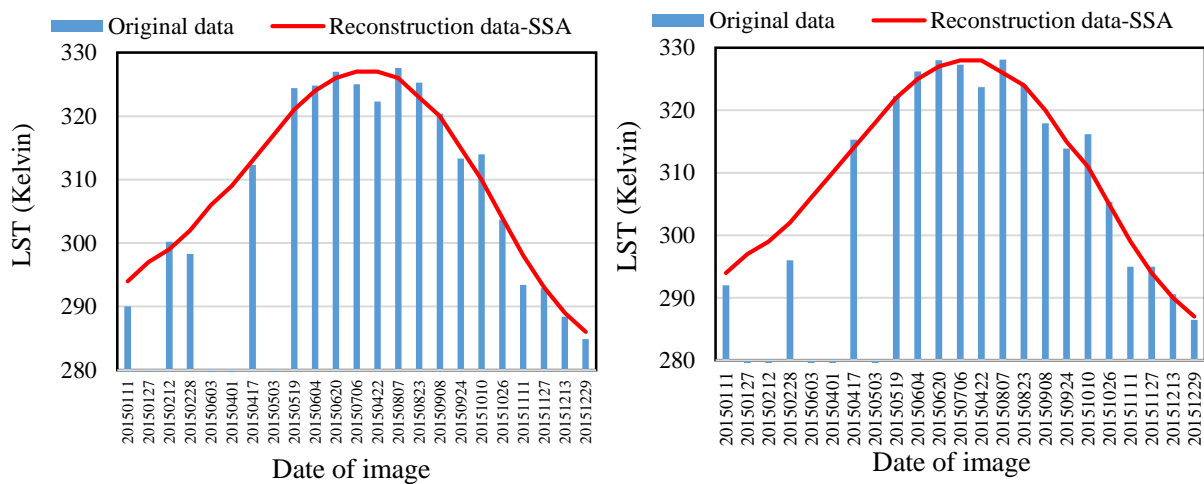

Fig. 7. Reconstruction results of two annual LST time series by SSA algorithm

Figure 8 shows the RMSE and MAE maps between the original data (without cloud cover) and reconstructed data by SSA. As indicated, the minimum RMSE is 1.8 K and its maximum value is 5.7 K, with a mean of 3.4 K. Based on the RMSE histogram, the highest frequency of RMSE is 2.5-4 K (Fig. 9, left). According to Fig. 8, the minimum MAE is 1.3 K and maximum MAE is 4.3 K, with a mean of 2.5 K. Moreover, the highest frequency of MAE is 2-3 K (Fig. 9, right). Figure 10 illustrates two samples of reconstructed images by SSA algorithm on 2015/05/19 and 2015/02/12.

As explained in the materials and methods section, original data are required to determine the gap-filling error. Original data are invalid or nonexistent in cloudy images. To determine the gap-filling error, five images without cloud cover in four iterations were extracted from the time series and were then reconstructed by SSA algorithm. Finally, the RMSE and MAE between the five original images and reconstructed images were determined in four iterations and then the final mean map of the mentioned errors was calculated. Figure 11 indicates the RMSE and MAE in four iterations between the five extracted and reconstructed images by SSA algorithm. As shown in Fig. 11 (left), the minimum and maximum temporal RMSEs of the five original and reconstructed images were 2.1 and 6.7 K, respectively, with a mean of 4.4 K. Based on Fig. 11 (left), the highest frequency of RMSE is 3-6 K. According to Fig. 11 (right), the minimum MAE is 1.7 K and maximum MAE is 5.6 K, with a mean temporal error of 3.6 K. Further, the highest frequency of MAE is 3-5 K (Fig. 12, right).
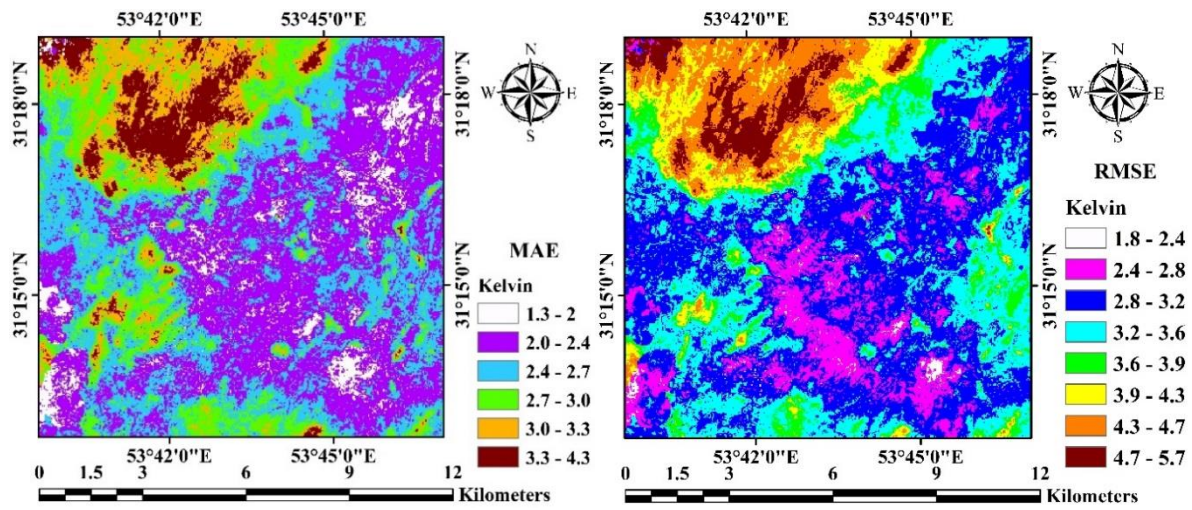
Fig. 8. RMSE (left) and MAE (right) maps between the original data and
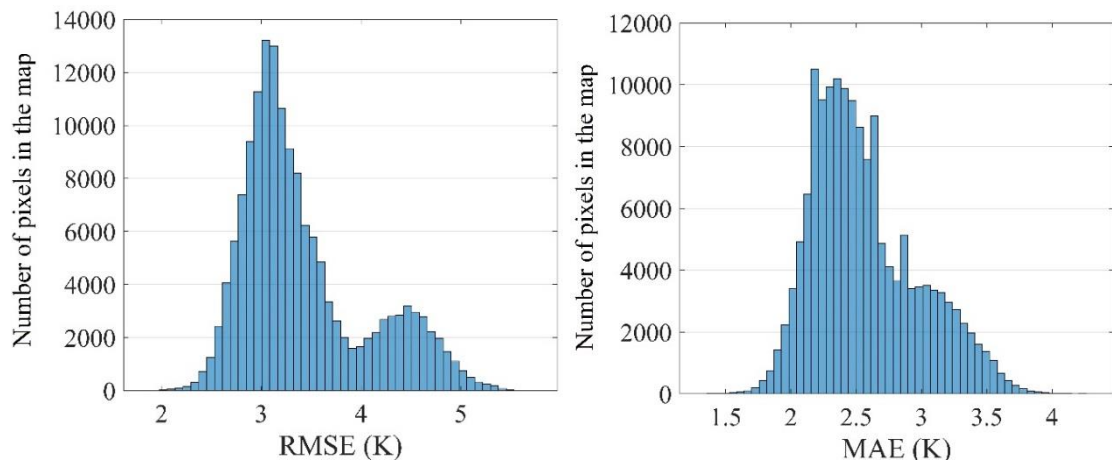data reconstructed by SSA algorithm

Fig. 9. Histogram of RMSE (left) and MAE (right) between the original data and data reconstructed by
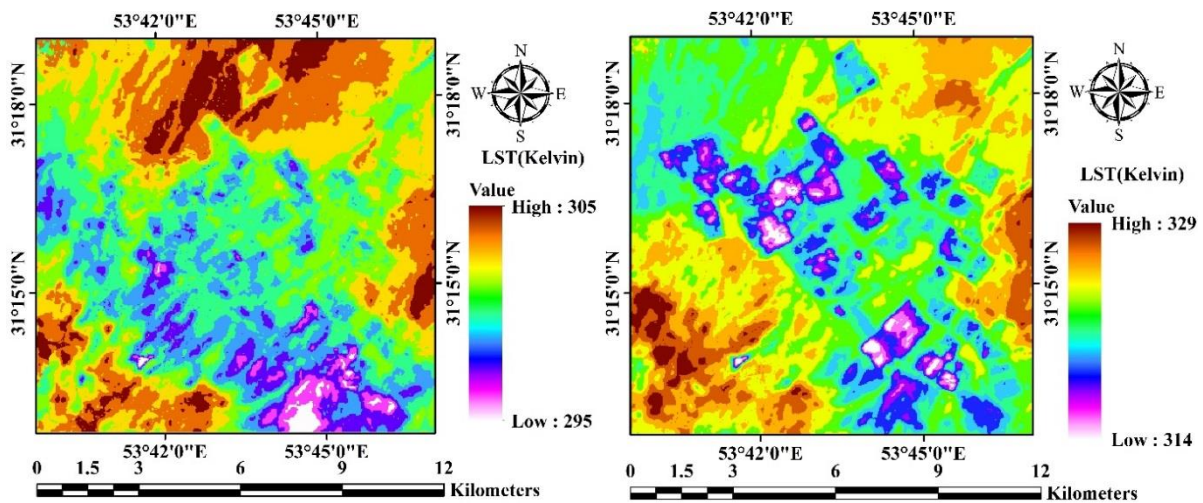SSA algorithm

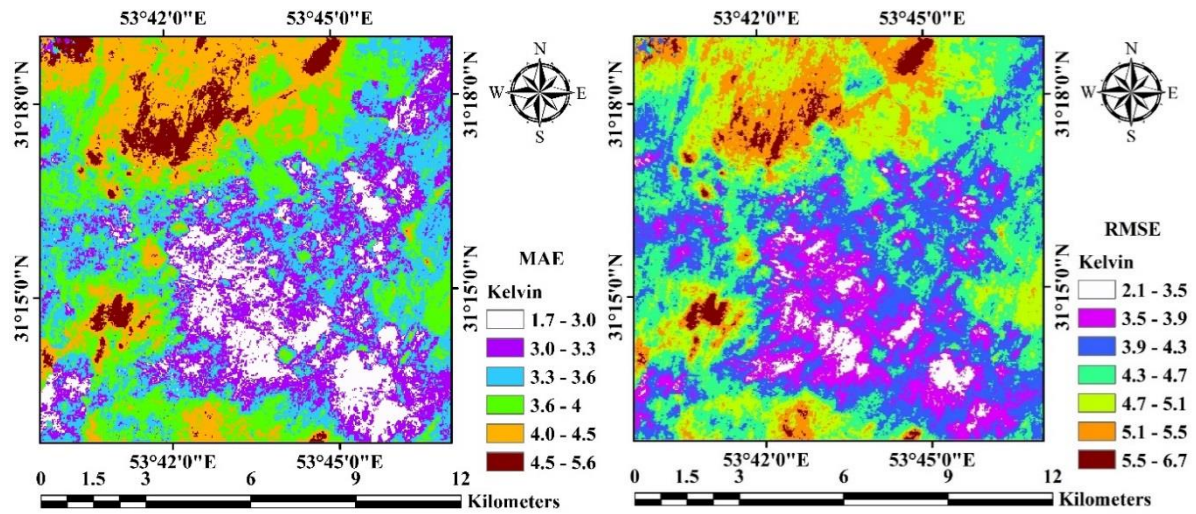**Fig. 10.** Two LST images reconstructed by SSA algorithm on 2015/05/19 (left) and 2015/02/12 (right)

Fig. 11. Temporal map of RMSE (left) and MAE (right) in four iterations between the five images extracted from and reconstructed by SSA algorithm
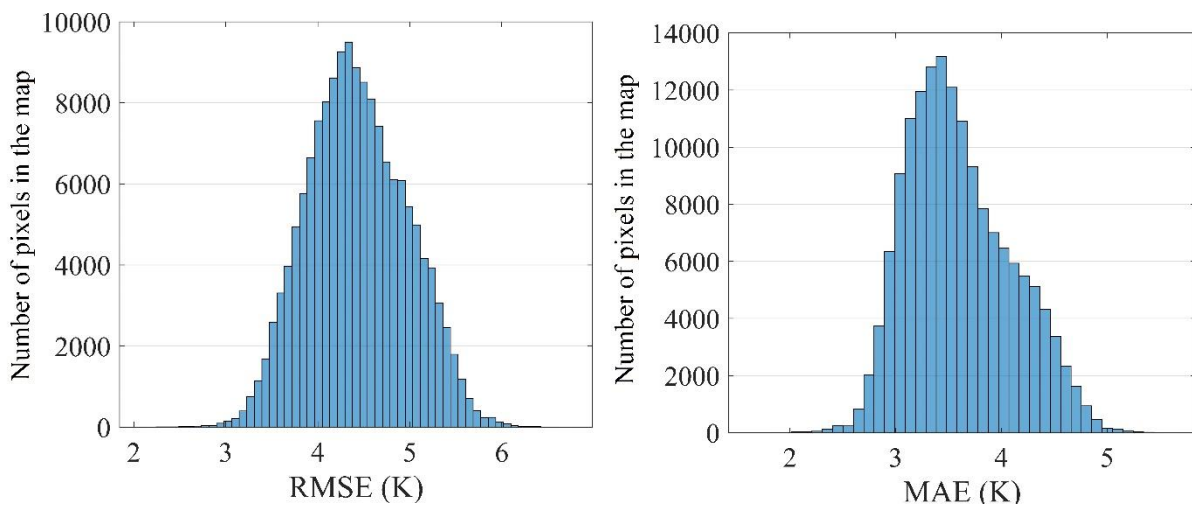

Fig. 12. Temporal histogram of RMSE (left) and MAE (right) in four iterations between the five images extracted from and reconstructed by SSA algorithm

The spatial RMSE and MAE of five randomly extracted and reconstructed images by SSA algorithm in four iterations are presented in Table 4. The reconstruction error varied in the random images extracted in different iterations. The lowest and highest RMSE and MAE rates within an image were found to be 1 and 9 K, respectively. The highest RMSE was recorded in random iteration 3 on 2015/01/11, which is due to the location of this image at the beginning of time series. The RMSE and MAE of the images on 2015/10/10, which occurred randomly in three iterations, were higher than those of other images. The reason for this is that the image on 2015/10/10 had a higher temperature than the images on the former and later dates. This high temperature was identified as outlier compared to the previous and later data (Fig. 7). The mean final RMSE and MAE within each image in four iterations with five extracted images were obtained to be 3.7 and 2.8 K.

Table 4. Spatial error in reconstruction of five random images extracted and reconstructed by SSA algorithm in four iterations

Random iteration	Image date	2015/06/20	2015/08/23	2015/10/10	2015/11/11	205/12/13	Mean
1	RMSE	1.5	4.2	6.0	7.8	5.1	4.9
	MAE	1.1	4.0	6.0	7.5	4.7	4.6
Random iteration	Image date	2015/04/17	2015/09/24	2015/10/10	2015/11/27	2015/12/29	Mean
2	RMSE	1.1	2.0	6.9	2.6	2.4	3.0
	MAE	0.9	1.6	6.7	2.1	2.1	2.7
Random iteration	Image date	2015/01/15	2015/06/04	2015/06/20	2015/09/08	2015/12/13	Mean
3	RMSE	9.0	4.1	2.4	1.2	1.8	3.7
	MAE	8.9	3.9	2.1	1.0	1.4	3.4
Random iteration	Image date	2015/04/17	2015/05/19	2015/08/07	2015/10/10	2015/10/26	Mean
4	RMSE	2.0	3.4	2.3	7.1	2.8	3.5
	MAE	1.8	3.3	2.0	7.1	2.7	3.4

4. Discussion

Various algorithms have been proposed for the estimation of LST from different sensors. These algorithms are based on various assumptions and approximations of the radiative transfer equation. In this research, the split window algorithm was used to calculate the LST using Landsat 8 images. Many researches in this field showed that the split window algorithm has a suitable accuracy in the field of land surface temperature estimation (Jiménez-Muñoz *et al*., 2014; Yu *et al*., 2014; Feizizadeh, *et al*., 2016; Rahimian *et al*.,2017; Wang *et al*., 2019; Jiang and Lin,2021).

In the present research, the SSA algorithm was used to reconstruct the missing data due to cloud cover in Landsat 8 LST time series during 2015. Two types of error occur during the reconstruction of time series. The first type of error is reconstruction error at data points and the second type of error is gap-filling error. The assessment of the accuracy of SSA algorithm in reconstruction of data points showed the RMSE and MAE of 3.4 and 2.5 K in the studied area, respectively. Moreover, the highest level of the frequencies in drawn histogram had an RMSE of 2.5-4 K. The reconstruction error of gaps was estimated using synthetic missing data as five images extracted from the time series and corresponding reconstructed images in four iterations.

The findings indicated mean temporal RMSE and MAE between the five extracted and reconstructed images were 4.4 and 3.6 K, respectively. The spatial RMSE and MAE in LST time series in four iterations with five extracted images were 3.7 and 2.8 K within each image. In general, reconstruction errors at data points and data-free points were located in an acceptable range because they were in line with the temperature estimation errors by remote sensing (±3 K) (Li *et al*., 2013). It should also be noted that the reconstruction error of gaps was estimated when the missing data increased approximately to 50% at all sampling points.

The highest spatial reconstruction error of gaps was observed in an image extracted from the beginning of the time series. The reconstruction error of time series can vary depending on the

amount, distribution, and dispersion of the missing data. When the missing data are located in the beginning and end of the time series, the reconstruction error will increase. However, it should be noted that this type of error can be reduced by taking a longer time series, e.g. reconstruction of a three-year time series instead of an annual time series. Moreover, the reconstruction error obtained in the current study can be reduced by decreasing the window size. The fitted curve will have more compatibility with the original data by decreasing the window size. Yet, it should be noted that this can be used based on the user's need and accuracy of original data. Therefore, increasing the window size generally elevates the spectral cover of SSA and provides more information about the original pattern of time series, while reducing the window size enhances the statistical reliability of the final results (Elsner and Tsonis, 1996).

Ghafarian and Zare Khormizi (2017) reconstructed daily MODIS LST time series by HANTS algorithm. Their results showed the reconstruction error in annual MODIS LST time series during the day in the study region was 3.87 K on average. Ghafarian Malamiri *et al*. (2018) studied the capacity of SSA algorithm in the reconstruction of missing data due to cloud cover in daily MODIS LST time series using 730 data and reported an RMSE of 2.95 K between the original and reconstructed data. In another study, Ghafarian *et al* (2020) investigated the performance of HANTS and SSA algorithms in reconstructing long-gap missing data in NDVI time series. The results of this study showed that M-SSA algorithm is more accurate than HANTS. HANTS algorithm only uses temporal interpolation between observations for the reconstruction of time series, while SSA algorithm makes use of spatio-temporal interpolation in M-SSA for reconstruction of time series. On the other hand, in addition to temporal interpolation for reconstruction of time series, the same time series is compared with all processing matrix time series and is included in the results of reconstruction of the first time series based on the highest correlation. Hence, the final accuracy will be better in SSA algorithm than in HANTS algorithm, especially in time series with long missing data.

In a study, Ghafarian Malamiri (2015) created missing data and noise with different percentage, distribution, and dispersion in a time series with a length of 177, width of 102 pixels, and 744 hourly temporal LST images and showed that when the missing data is 60-70%, RMSE in reconstruction of these time series by SAA varies from 1 to 4 K depending on the noise created.

The results of Monte Carlo test in annual TRIS LST time series of Landsat 8 showed two significant components at 97.5% level. These two components indicated annual cycles of temperature change in an annual time series, which was used for reconstruction of annual LST time series in the studied region. The time series have various components (cycle or trend) depending on the number of sampled temporal data. Ghafarian Malamiri (2015) conducted a study on the reconstruction of hourly LST time series in 72-hour window size and differentiated three significant cyclic components of 8, 12, and 24 hours using SSA software. In another study, Ghafarian Malamiri (2018) identified three significant components in daily MODIS LST time series with day-night sequence. The first component showed the day-night temperature variations, the second component indicated annual temperature variations, and the third component showed seasonal temperature variations.

Based on the results, the SSA algorithm can be helpful in resolving the missing data problem in Landsat 8 LST time series. A study showed M-SSA can efficiently reconstruct MODIS Leaf Area Index (LAI) using spatio-temporal correlation (Wang and Liang., 2008). In another study, Ghafarian *et al*. (2012) reconstructed the hourly data of LST time series by SSA and M-SSA algorithms. They reported an MAE of 2.25 K for hourly time series images with mean missing data of 63% due to cloud cover. In general, SSA algorithm can be effectively used to resolve the problem of missing data due to cloud cover in Landsat 8 LST time series.

5. Conclusion

In the present study, the split-window algorithm was used to estimate LST using Landsat 8 images during 2015. Clouds are one of the most important factors in creating lost (Gap) and outlier data in time series of land surface temperature. In this research, using the M-SSA algorithm, the gaps created by the cloud cover were effectively reconstructed. However, it should be noted that the reconstructed data in this study was created assuming the absence of clouds. The estimation of LST during the cloud coverages are depended on many factors such as cloudy hours, time of the days, duration of cloudiness, season, topography, soil moisture, texture, ground coverage type, soil thermal properties and soil thermal inertia (admittance), etc. Estimating the land surface temperature under the cloud can be a challenge and suggestion for further studies.

References

Ackerman, S. A., K. I. Strabala, W. P. Menzel, R. A. Frey, C. C. Moeller, & L. E. Gumley, 2006. Discriminating clear sky from clouds with MODIS. Journal of Geophysical Research, 103; 32141-32157.

Broomhead, D. S., & G. P. King, 1986. Extracting qualitative dynamics from experimental data. Physica D: Nonlinear Phenomena, 20; 217-236.

Cai, Z,, P. Jönsson, H, Jin, & L. Eklundh, 2017. Performance of smoothing methods for reconstructing NDVI time-series and estimating vegetation phenology from MODIS data. Remote Sensing, 9 (12); 1271.

Chen, D., Q. Zhuang, L. Zhu, & W. Zhang, 2022. Comparison of Methods for Reconstructing MODIS Land Surface Temperature under Cloudy Conditions. Applied Sciences, 12(12); 6068.

Costa, J, D, O., R. D. Coelho, W. Wolff, J. V. José, M. V. Folegatti, & S. F. Ferraz, 2019. Spatial variability of coffee plant water consumption based on the SEBAL algorithm. Scientia Agricola, 76(2); 93-101.

Du, C., H. Ren, Q. Qin, J. Meng, & S. Zhao, 2015. A practical split-window algorithm for estimating land surface temperature from Landsat 8 data. Remote Sensing, 7(1); 647-665.

Elsner, J. B., & A. A. Tsonis, 1996. Singular Spectrum Analysis: A New Tool in Time Series Analysis. New York. USA: Plenum Press.

Estes, M. G., M. Z. Al-Hamdan., W. Crosson, S. M. Estes, D. Quattrochi, S. Kent, & L. A. McClure, 2009. Use of remotely sensed data to evaluate the relationship between living environment and blood pressure. Environ Health Perspect, 117 (12); 1832-1838.

Feizizadeh, B., K. Didehban, & K. Gholamnia, 2016. Extraction of Land Surface Temperature (LST) based on Landsat Satellite Images and Split Window Algorithm Study area: Mahabad Catchment. Scientific- Research Quarterly of Geographical Data (SEPEHR), 25(98); 171-181.

Geng, L., M. Ma, X. Wang, W. Yu, S. Jia, & H. Wang, 2014. Comparison of Eight Techniques for Reconstructing Multi-Satellite Sensor Time-Series NDVI Data Sets in the Heihe River Basin, China. Remote Sensing, 6(3); 2024–2049.

Ghafarian, H. R., M. Menenti, L. H. Jia, & R. den Ouden, 2012. Reconstruction of cloud-free time series satellite observations of land surface temperature. In, EARSeL eProceedings (pp. 121-131)

Ghafarian Malamiri, H. R., 2015. Reconstruction of gap-free time series satellite observations of land surface temperature to model spectral soil thermal admittance (Doctoral dissertation), Technische Universiteit Delft, The Netherlands.

Ghafarian Malamiri, H. R., H. Zare, I. Rousta, H. Olafsson, E. Izquierdo Verdiguier, H. Zhang, & T. D. Mushore, 2020. Comparison of harmonic analysis of time series (HANTS) and multi-singular spectrum analysis (M-SSA) in reconstruction of long-gap missing data in NDVI time series. Remote Sensing, 12(17); 2747.

Ghafarian Malamiri, H. R., & H. Zare Khormizi, 2017. Reconstruction of cloud-free time series satellite observations of land surface temperature (LST) using harmonic analysis of time series algorithm (HANTS). Journal of RS and GIS for Natural Resources, 8(3); 37-55.

Ghafarian Malamiri, H. R., & H. Zare Khormizi, 2020. Investigating vegetation changes in Iran using NDVI time series of NOAA-AVHRR sensor and Harmonic ANalysis of Time Series (HANTS). Scientific- Research Quarterly of Geographical Data (SEPEHR), 29(113); 141-158.

Ghafarian Malamiri, H., I. Rousta, H. Olafsson, H. Zare, & H. Zhang, 2018. Gap-Filling of MODIS Time Series Land Surface Temperature (LST) Products Using Singular Spectrum Analysis (SSA). Atmosphere, 9(9); 334.

Ghil, M., M. R. Allen, M. D. Dettinger, K. Ide, D. Kondrashov, M. E. Mann, ... , & P. Yiou, 2002. Advanced spectral methods for climatic time series. Reviews of geophysics, 40(1); 3-1.

Ghil, M., & R. Vautard, 1991. Interdecadal oscillations and the warming trend in global temperature time series. NATURE, 350; 324-327.

Golyandina, N., V. Nekrutkin, & A. Zhigljavsky, 2001. Analysis of Time Series Structure: SSA and Related Techniques. Washington DC, USA: CHAPMAN &HALL/CRC

Golyandina, N., & A. Zhigljavsky, 2013. Singular Spectrum Analysis for Time Series: SpringerBriefs in Statistics.

Irons, J. R., J. L. Dwyer, & J. A. Barsi, 2012. The next Landsat satellite: The Landsat data continuity mission. Remote Sensing of Environment, 122; 11-21.

Izquierdo Verdiguier, E., 2014. Kernel Feature Extraction Methods for Remote Sensing Data Analysis. University of Valencia, Spain.

Jiang, Y., & W. Lin, 2021. A comparative analysis of retrieval algorithms of land surface temperature from Landsat-8 data: a case study of Shanghai, China. International Journal of Environmental Research and Public Health, 18(11); 5659.

Jiménez-Muñoz, J. C., J. A. Sobrino, D. Skoković, C. Mattar, & J. Cristóbal, 2014. Land surface temperature retrieval methods from Landsat-8 thermal infrared sensor data. IEEE Geoscience and Remote Sensing Letters, 11(10); 1840-1843.

Johnson. B., R. Tateishi, & T. Kobayashi,   2012. Remote sensing of fractional green vegetation cover using spatially-interpolated endmembers. Remote Sensing, 4(9); 2619-2634.

Julien, Y., & J. A. Sobrino, 2010. Comparison of cloud-reconstruction methods for time series of composite NDVI data. Remote Sensing of Environment, 114; 618-625.

Julien, Y., J. A. Sobrino, & W. Verhoef, 2006. Changes in land surface temperatures and   NDVI values over Europe between 1982 and 1999. Remote Sensing of Environment,   103(1); 43-55.

Kondrashov, D., & M. Ghil, 2006. Spatio-temporal filling of missing points in geophysical data sets. Nonlinear Processes in Geophysics, 13; 151-159.

Kondrashov, D., Y. Shprits, & M. Ghil, 2010. Gap filling of solar wind data by singular spectrum analysis. Geophysical research letters, 37(15).

Latif, M. S., 2014. Land Surface Temperature Retrieval of Landsat-8 Data Using Split Window Algorithm-A Case Study of Ranchi District. International Journal of Engineering Development and Research, 2(4); 2840-3849.

Li, J., B. E. Carlson, & A. A. Lacis, 2013. Application of spectral analysis techniques in the intercomparison of aerosol data: 1. An EOF approach to analyze the spatial-temporal variability of aerosol optical depth using multiple remote sensing data sets. Journal of Geophysical Research: Atmospheres, 118; 8640-8648.

Li, Z. L., L. Jia, Z. Su, Z. Wan, & R. Zhang, 2003. A new approach for retrieving precipitable water from ATSR2 split-window channel data over land area. International Journal of Remote Sensing, 24(24); 5095-5117.

Menenti, M., S. Azzali, W. Verhoef, & R. Van Swol, 1993. Mapping agroecological zones and time lag in vegetation growth by means of Fourier analysis of time series of NDVI images. Advances in Space Research, 13; 233-237.

Mukherjee, S., P. K. Joshi, & R. D. Garg, 2014. A comparison of different regression models for downscaling Landsat and MODIS land surface temperature images over heterogeneous landscape. Advances in Space Research, 54; 655-669.

Musial, J. P., M. M. Verstraete, & N. Gobron, 2011. Comparing the effectiveness of recent algorithms to fill and smooth incomplete and noisy time series. Atmospheric chemistry and physics, 11(15); 7905-7923.

Rahimian, M. H., M. shayannejad, S. Eslamian, R. Jafari, M. Gheysari, & S. Taghvaeian, 2017. Evaluation of different LST approaches for determination of pistachio tree canopy temperature through Landsat 8 satellite data. Journal of Geospatial Information Technology, 5 (2); 79-98.

Rouse, J. W., R. H. Haas, J. A. Schell, & D. W. Deering, 1973. Monitoring vegetation systems in the Great Plains with ERTS. In 3rd ERTS Symposium, NASA SP-351 I; 309-317.

Sajib, M. Q. U., & T. Wang, 2020. Estimation of Land Surface Temperature in an agricultural region of Bangladesh from Landsat 8: Intercomparison of four algorithms. Sensors, 20(6); 1778.

Schoellhamer, D. H., 2001. Singular spectrum analysis for time series with missing data. Geophysical research letters, 28(16); 3187-3190.

Sekertekin, A., & S. Bonafoni, 2020. Land surface temperature retrieval from Landsat 5, 7, and 8 over rural areas: Assessment of different retrieval algorithms and emissivity models and toolbox implementation. Remote sensing, 12(2); 294.

Skoković, D., J. A. Sobrino, J. C. Jimenez-Munoz, G. Soria, Y. Julien, C. Mattar, & J. Cristobal, 2014. Calibration and validation of land surface temperature for Landsat 8-TIRS sensor. Land product Validation and Evolution, ESA/ESRIN Frascati (Italy); 9-6.

Sobrino, J. A., J. C. Jiménez-Muñoz, G. Sòria, M. Romaguera, L. Guanter, J. Moreno, ... , & P. Martínez, 2008. Land surface emissivity retrieval from different VNIR and TIR sensors. IEEE Transactions on Geoscience and Remote Sensing, 46(2); 316-327.

Sobrino, J. A., J. E. Kharraz, & Z. L. Li, 2003. Surface temperature and water vapour etrieval from MODIS data. International Journal of Remote Sensing 24(24); 5161-5182.

Sobrino, J. A., Z. L. Li, M. P. Stoll, & F. Becker, 1996. Multi-channel and multi-angle algorithms for estimating sea and land surface temperature with ATSR data. International Journal of Remote Sensing, 17(11); 2089-2114.

Sun, D. L., R. T. Pinker, & J. B. Basara, 2004. Land surface temperature estimation from the next generation of Geostationary Operational Environmental Satellites: GOES M-Q. Journal of Applied Meteorology, 43 (2); 363-372.

Tatem, A. J., S. J. Goetz, & S. I. Hay, 2004. Terra and Aqua: new data for epidemiology and public health. International Journal of Applied Earth Observation and Geoinformation, 6 (1); 33-46.

Teixeira, A. H. D. C., 2010. Determining regional actual evapotranspiration of irrigated crops and natural vegetation in the São Francisco river basin (Brazil) using remote sensing and Penman-Monteith equation. Remote Sensing, 2(5); 1287-1319.

Vautard, R., & M. Ghil, 1989. Singular spectrum analysis in nonlinear dynamics, with applications to paleoclimatic time series. Physica D: Nonlinear Phenomena, 35; 395-424.

Vautard, R., P. Yiou, & M. Ghil, 1992. Singular-spectrum analysis: A toolkit for short, noisy chaotic signals. Physica D: Nonlinear Phenomena, 58(1-4); 95-126.

Verhoef, W., 1996. Application of Harmonic Analysis of NDVI Time Series (HANTS). In S. Azzali & M. Menenti (Eds.), In: Fourier analysis of temporal NDVI in southern Africa and America continent. (pp. 19-24). Wageningen (The Netherlands): Dlo Winand Staring Center.

Verhoef, W., M. Menenti, & S. Azzali, 1996. Cover A colour composite of NOAA AVHRR- NDVI based on time series analysis (1981-1992). International Journal of Remote Sensing, 17; 231-235.

Wang, D., & S, Liang, 2008. Singular Spectrum Analysis for Filling Gaps and Reducing Uncertainties of MODIS Land Products. Geoscience and Remote Sensing Symposium, 2008. IGARSS 2008. IEEE International.

Wang, F., Z. Qin, C. Song, L. Tu, A. Karnieli, & S. Zhao, 2015. An improved mono-window algorithm for land surface temperature retrieval from Landsat 8 thermal infrared sensor data. Remote Sensing, 7(4); 4268-4289.

Wang, L., Y. Lu, & Y. Yao, 2019. Comparison of three algorithms for the retrieval of land surface temperature from Landsat 8 images. Sensors, 19(22); 5049.

Xu, Y., & Y. Shen, 2013. Reconstruction of the land surface temperature time series using harmonic analysis. Computers & Geosciences, 61; 126-132.

Yiou, P., E. Baert, & M. F. Loutre, 1996. Spectral analysis of climate data. Surveys in Geophysics, 17; 619-663.

Yiou, P., D. Sornette, & M. Ghil, 2000. Data-adaptive wavelets and multi-scale singularspectrum analysis. Physica D, 142; 254-290.

Yu, X., X. Guo, & Z. Wu, 2014. Land surface temperature retrieval from Landsat 8 TIRS-Comparison between radiative transfer equation-based method, split window algorithm and single channel method. Remote Sensing, 6 (10); 9829-9852.

Zare khormizi, H., S. Z. Hosseini, M. H. Mokhtari, & H. R. Ghafarian Malamiri, 2017. Reconstruction of MODIS NDVI Time Series using Harmonic AN alysis of Time Series algorithm (HANTS). The Journal of Spatial Planning, 21 (3); 221-255.

Zare khormizi, H., & H. R. Ghafarian Malamiri, 2020. Effect of height and temperature on plant phenological processes using harmonic analysis of MODIS NDVI time series (Case study: Shirkouh, Yazd province). Iranian Journal of Remote Sensing & GIS, 12(3); 1-22.

Zhou, J., L. Jia, & M. Menenti, 2015. Reconstruction of global MODIS NDVI time series: Performance of Harmonic ANalysis of Time Series (HANTS). Remote Sensing of Environment, 163(15); 217-228.

Zhou, J., L. Jia, M. Menenti, & B. Gorte, 2016. On the performance of remote sensing time series reconstruction methods–A spatial comparison. Remote Sensing of Environment, 187; 367-384.